Contents

摘要 I

Abstract IV

誌謝 VIII

Contents IX

Table Captions XIII

Figure Captions XIII

Chapter 1 Introduction

1-1. Introduction to the Ferroelectric Materials and Its Application on Nonvolatile Memory ……………………………………………………1

1-2. Introduction to the Hysteresis Measurement of Ferroelectric Materials ……………………………………………………………10

1-3. Motivation ……………………………………………………………13

1-4. Thesis Outline ………………………………………………………14

Chapter 2 Experimental Details

2-1. DC sputtering Deposition……………………………………………16

2-2. Dual E-gun Deposition………………………………………………16

2-3. Thermal Evaporation Deposition……………………………………16

2-4. Preparation of $Pb(Zr,Ti)O_3$ Precursor Solution……………………17

2-5. Deposition Procedures of Ferroelectric Capacitor……………………18

2-6. X-Ray Diffraction Analysis (XRD)…………………………………19

2-7. n&k Optical Analysis....................19
2-8. Atomic Force Microscope (AFM)....................19
2-9. Secondary Ion Mass Spectroscopy (SIMS)....................19
2-10. Auger electron spectrometry (AES)....................19
2-11. Thermal Desorption Spectra (TDS)....................19
2-12. Capacitance-Voltage Measurements (CV)....................19
2-13. Capacitance-Frequency Measurements (CF)....................20
2-14. Current-Voltage Measurements (IV)....................20
2-15. Polarization-Voltage Measurements (P-V)....................20
2-16. System of Capacitance Retention and Endurance Measurements......21
2-17. Capacitance Retention Measurements for MFIS Structure............22
2-18. Endurance Measurements for MFIS Structure....................23

Chapter 3 Low-Pressure Crystallization of Sol-Gel-Derived $PbZr_{0.52}Ti_{0.48}O_3$ Thin Films at Low Temperature for Low-Voltage Operation

3-1 Introduction 24
3-2. Experiments 25
3-3. Results and Discussions 25
3-3-1. Ferroelectric property 26
3-3-2. Crystallinity and Surface morphology 27
3-3-3. Interdiffusion property 28
3-3-4. Thermal desorption property....................30
3-3-5. Leakage property 31
3-3-6. Dielectric Property 32

3-3-7. Retention Property 37
3-4. Summary 38

Chapter 4 Basic Characteristics of $Pt/SrBi_2Ta_2O_9/HfO_2/Si$ Structure using Layer-By-Layer Crystallization

4-1. Introduction..39
4-2. Experiments..39
4-3. Results and Discussions.. 40
4-3-1. Characteristics of $Al/HfO_2/Si/Al$ MIS structure..41
4-3-2. Crystallinity and surface morphology of $SrBi_2Ta_2O_9/HfO_2/Si$ structure..44
4-3-3. Electrical properties of $Pt/SrBi_2Ta_2O_9/Pt/Ta/SiO_2/Si$ MFM and $Pt/SrBi_2Ta_2O_9/HfO_2/Si/Al$ MFIS structures..46
4-3-4. Inter-diffusion phenomena of $SrBi_2Ta_2O_9/HfO_2/Si$ stack..51
4-3-5. Endurance characteristics of $Pt/SrBi_2Ta_2O_9/ HfO_2/Si/Al$ MFIS structure..53
4-4. Summary 55

Chapter 5 Direct Measurement of Electrical Hysteresis of Micron- Sized $Pb(Zr,Ti)O_3$ Capacitors using the Constant Current Method

5-1. Introduction 56
5-2. Experiments 56
5-3. Results and Discussions..57
5-3-1. Verification of CC method..57
5-3-2. Hysteresis measurement of micron-sized ferroelectric capacitor..59

5-4. Summary……………………...………………………………….64

Chapter 6 Triangular Current: Method for Measuring Hysteresis Loops of Ferroelectric Capacitors and Its Application

6-1. Introduction………………………………………….……………65

6-2. Experiments…………………………...……….………………..…66

6-3. Results and Discussions…………………………………… 66

6-3-1. Verification of triangular current method…………...……………66

6-3-2. Effect on step charging current and number of step…………....69

6-3-3. Hysteresis measurement of micron-sized PZT capacitor…………70

6-3-4. Hysteresis measurement of MIS structure…………..……...……72

6-3-5. Hysteresis measurement of MFIS structure……………...………75

6-3-6. Temperature effect of hysteresis measurement of ferroelectric capacitor…………………………………...…………………..…77

6-4. Summary……………………...…………………………………..…80

Chapter 7 Switching Current Study: Hysteresis Measurement of Ferroelectric Capacitors using Current-Voltage Measurement Method

7-1. Introduction …………………………………...…………………81

7-2. Experiments ………………...…………………………………………82

7-3. Results and Discussions ……………………………………83

7-3-1. Verification of hysteresis loops ………...……………………...……83

7-3-2. Studies of full-switching and non-switching current…...………..87

7-3-3. Study of dynamic switching current in retention duration………89

7-3-4. Switching current characteristics for various depolarized bias….93

7-3-5. Temperature effect of switching current characteristics and P-V loops ……..94
7-4. Summary………………………….……………………..………...99

Chapter 8 Conclusions ………………..…………..……………………..100
References ………………………..…………………………………….103
Autobiography…………………………..………………………………..108
Publication List……………………..……………………………………109

Table Captions

Table 3-1 **The coercive voltage obtained from C-V and P-V measurements, for the Pt/$PbZr_{0.52}Ti_{0.48}O_3$/Pt capacitors annealed at various oxygen pressures.** (p. 34)

Table 3-2 **The reversible and total polarizations at 2.5 V, for the PZT thin films annealed at various oxygen pressures.** (p. 35)

Figure Captions

Chapter 1

Fig. 1-1. Perovskite crystal structure, having the atomic composition of ABO_3, where A represents a cation with a larger ionic radius. B represents a cation with a smaller radius, and O is oxygen. (Ref. [03], p. 2)

Fig. 1-2. (a) Ferroelectric materials exhibit spontaneous polarization with applied voltage due to the atomic displacement of the body-center atom in the perovskite structure (See Fig. 1-1). The polarization- voltage curve has two stable states at zero voltage after the removal of the field. (b) The energy potential-atomic displacement plot of ferroelectric material. (Ref. [04], p. 3)

Fig. 1-3. Circuit scheme of one-transistor/one-capacitor (1T/1C) designed FeRAM. (Ref. [07], p. 4)

Fig. 1-4. Circuit scheme of two-transistor/two-capacitor (2T/2C) designed FeRAM. (Ref. [07], p. 4)

Fig. 1-5. Timing diagram of the writing operation of 1T1C FeRAM. (a) Writing for logic "1" and (b) Writing for logic "0". (Ref. [07], p. 5)

Fig. 1-6. (a) Hysteresis loop of the ferroelectric capacitor. (b) Charge density to voltage characteristics of ferroelectric capacitor. (Ref. [07], p. 6)

Fig. 1-7. Timing diagram of the reading operation of 1T1C FeRAM. (a) Reading logic ”1” and (b) Reading logic “0”. (Ref. [07], p. 7)

Fig. 1-8. BL capacitance (C_{BL}) dependence of sense margin for 1T1C FeRAM. (p. 7)

Fig. 1-9. Circuit schemes of (a) conventional and (b) chain 1T1C FeRAM. (c) Scheme of cross-section view of chain FeRAM. (Ref. [08-10], p. 8)

Fig. 1-10. Structure of 1T FeRAM: (a) MFIS FET and (b) MFMIS FET. (Ref. [04], p. 9)

Fig. 1-11. Scheme of Sawyer-Tower circuit and setup to trace hysteresis loops. (Ref. [24], p. 10)

Fig. 1-12. Scheme of shunt method and setup to trace switching current. (Ref. [25], p. 11)

Fig. 1-13. Pulse sequence used to measure switching currents of ferroelectric capacitors (a five-pulses method). (Ref. [03],p. 12)

Fig. 1-14. Switchable current and non-switching current characteristics of ferroelectric capacitors. (Ref. [03],p. 12)

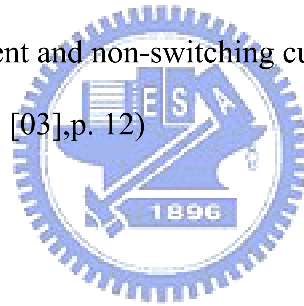

Chapter 2

Fig. 2-1 Procedures of precursor preparation of PZT ferroelectric materials using the sol-gel method. (p. 17)

Fig. 2-2 Deposition procedures of ferroelectric film using the sol-gel method or MOD technique. (p. 18)

Fig. 2-3 MFM and MFIS capacitor structures for the measurements. (p. 20)

Fig. 2-4 Schematic system construction for performing the capacitance retention measurement and endurance measurement of the MFIS structure. (p. 21)

Fig. 2-5 Measurement procedure of the capacitance retention property for the MFIS structure. (p. 22)

Fig. 2-6 Measurement procedure of the capacitance retention property for the MFIS structure. (p. 23)

Chapter 3

Fig. 3-1. *P-E* hysteresis loops of PZT thin films annealed in various oxygen pressures, (a) 1atm, (b) 200mbar, and (c) 60mbar. All samples were annealed at 500°C for 15min. (p. 26)

Fig. 3-2. Surface morphologies of PZT thin films annealed in various oxygen pressures and temperatures, (a) 1 atm, 500°C for 15 min, (b) 200 mbar, 500°C for 15 min, (c) 60mbar, 500°C for 15 min, and (d) 1 atm, 550°C for 5 min. (p. 27)

Fig. 3-3. X-ray diffraction patterns of PZT thin films annealed in various oxygen pressures at 500°C for 15min. (p. 28)

Fig. 3-4. AES depth profiles of as-deposited PZT thin films and those annealed in various oxygen pressures. All samples were annealed at 500°C for 15 min. (p. 29)

Fig. 3-5. TDS spectra of the PZT thin films annealed in various oxygen pressures. All samples were annealed at 500°C for 15 min. (p. 30)

Fig. 3-6. Leakage current density-voltage characteristics of the PZT thin films annealed in various oxygen pressures. All samples were annealed at 500°C for 15 min. (p. 31)

Fig. 3-7. Frequency-dependent dielectric properties of the PZT thin films annealed in various oxygen pressures. The signal level was about 50 mV. The frequency ranged form 100 Hz to 100 kHz. All samples were annealed at 500°C for 15 min. (p. 32)

Fig. 3-8. Capacitance-voltage characteristics of the PZT thin films annealed in various oxygen pressures. The measurement frequency was kept at 100 kHz. The applied bias may be ranged from ±2.5 V and the signal level was fixed at 50

mV. All samples were annealed at 500°C for 15 min. (p. 33)

Fig. 3-9. P-V properties of the PZT thin films annealed in various oxygen pressures. The applied bias may be ranged from ±2.5 V. The frequency was around 56 Hz. All samples were annealed at 500°C for 15 min. (p. 34)

Fig. 3-10. (a) Reversible polarization of the PZT thin films annealed in various oxygen pressures. (b) Comparison of the reversible to total polarization for the sample annealed at the oxygen pressure of around 60 mbar. The reversible polarizations were obtained by integrating the C-V curves shown in Fig. 3-9. (p. 36)

Fig. 3-11. Retention properties of the PZT thin films annealed in various oxygen pressures. The pulse width of write and read pulses were around 2 ms. The amplitudes of write and read pulses were around 3 V. All samples were annealed at 500°C for 15 min. (p. 37)

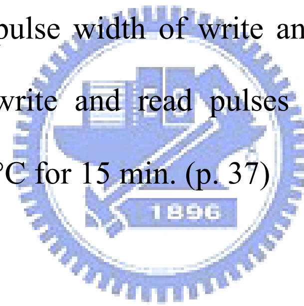

Chapter 4

Fig. 4-1 Current-voltage characteristic of Al/HfO_2/Si capacitor annealed at various PDA temperatures in oxygen ambient. The annealing time was about 180 s. (p. 41)

Fig. 4-2 Capacitance-frequency characteristic of Al/HfO_2/Si capacitor annealed at various PDA temperatures in oxygen ambient. The annealing time was about 180 s. (p. 42)

Fig.4-3 AFM images of HfO_2/Si structure: (a) asdeposited film and (b) the film annealed at PDA temperature of 900 °C for 180 s in oxygen ambient. (p. 42)

Fig. 4-4 XRD patterns of HfO_2/Si structure with 14-nm-thick HfO_2 films as a function

of the PDA temperature. The HfO_2 film was annealed at 900 ^oC for 180 s in oxygen ambient. (p. 43)

Fig. 4-5 (a) Capacitance-voltage and (b) Current density-voltage characteristics of Al/HfO2/Si capacitor. The inset shows the capacitance-frequency characteristic of this capacitor. (p. 44)

Fig. 4-6 XRD patterns of SBT/HfO_2/Si structure with conventionally crystallized and layer-by-layer-crystallized SBT films as a function of the PDA temperature. (p. 45)

Fig. 4-7 AFM images of layer-by-layer-crystallized SBT/HfO_2/Si structure: (a) as-deposition, (b) PDA temperature of 750 ^oC and (c) PDA temperature of 850 ^oC. (d) Surface roughness of conventionally crystallized (full circles) and layer-by-layer-crystallized (open squares) SBT/HfO_2/Si structures as a function of PDA temperature. (p. 46)

Fig. 4-8 Capacitance-voltage characteristics of (a) conventionally crystallized (circles) and (b) layer-by-layer-crystallized (squares) Pt/SBT/HfO_2/Si structures. The open and full symbols represent the results of MFIS structure annealed at the PDA temperature of 750 ^oC and 850 ^oC. (p. 47)

Fig. 4-9 Current density-voltage characteristics of conventionally crystallized (circles) and layer-by-layer-crystallized (squares) Pt/SBT/HfO_2/Si structures. The open and full symbols represent the results of MFIS structure annealed at the PDA temperature of 750 ^oC and 850 ^oC. (p. 48)

Fig. 4-10 Current density-voltage characteristics of conventionally crystallized (dashed line) and layer-by-layer-crystallized (solid line) Pt/SBT/Pt/ Ta/SiO_2/Si MFM capacitors annealed at PDA temperature of 750 ^oC. (p. 49)

Fig. 4-11 Ln(J)-$V^{1/2}$ (full symbol) and Ln(J/V)-$V^{1/2}$ (open symbol) plots of (a) conventionally crystallized (circles) and (b) layer-by-layer-crystallized

(squares) Pt/SBT/Pt/Ta/SiO_2/Si MFM capacitors annealed at PDA temperature of 750 ^oC. (p. 50)

Fig. 4-12 Capacitance retention characteristics of conventionally crystallized and layer-by-layer-crystallized Pt/SBT/HfO_2/Si structure annealed at PDA temperature of 750 ^oC and 850 ^oC. $C_{Off}(t)$ and $C_{On}(t)$ represent the time-dependent capacitance as negative and positive write pulses was applied, respectively. The retention properties were measured at 0.0 V for layer-by-layer-crystallized MFIS structures, and at 0.7 V and 0.5 V for conventionally crystallized MFIS structures annealed at PDA temperature of 750 ^oC and 850 ^oC, respectively. (p. 51)

Fig. 4-13 SIMS depth profiles of (a) conventionally crystallized and (b) layer-by-layer-crystallized SBT/HfO_2/Si stacks annealed at PDA temperature of 850 ^oC for 180 s in oxygen ambient. (p. 52)

Fig. 4-14 SIMS depth profiles of conventionally crystallized SBT/HfO_2/Si stacks annealed at PDA temperature of 750 ^oC for 180 s in oxygen ambient. (p. 53)

Fig. 4-15 Memory window (open squares) and central voltage (full circles) as a function of switching cycles for layer-by-layer-crystallized Pt/SBT/ HfO_2/Si structure annealed at PDA temperature of 850 ^oC. (p. 54)

Fig. 4-16 C-V characteristics before (full squares) and after (solid line) 10^9 switching cycles for layer-by-layer-crystallized Pt/SBT/HfO_2/Si structure annealed at PDA temperature of 850 ^oC. The memory window of both curve were around 0.32 V. (p. 54)

Fig. 4-17 Capacitance retention characteristics before (solid line) and after (open circles) 10^9 switching cycles for layer-by-layer-crystallized Pt/SBT/ HfO_2/Si structure annealed at PDA temperature of 850 ^oC. The retention time exceeded 10^4 s and the extrapolated retention time was approximately 10^5 s. (p. 55)

Chapter 5

Fig. 5-1 Electric constant current array (dashed line) and resulting voltage (open circle) vs time plot, obtained using the constant current method, for a 250-nm-thick PZT(30/70) film. (p. 58)

Fig. 5-2 Current-voltage characteristics and the ratio I/I_0 for a 250-nm-thick PZT(30/70) film, where $I_0 = 20nA$ is the testing constant current. (p. 58)

Fig. 5-3 Hysteresis curves of electric displacement ***D*** vs voltage ***V***. The unbroken line plots the curve obtained by the virtual ground method (VGM); the open circles represent results obtained using the constant current method (CCM). The area of the sample was 10^{-4} cm^2. (p. 59)

Fig. 5-4 Hysteresis plots obtained from 100μm×100μm, 50μm×50μm, 20μm×20μm, 10μm× 10μm, 5μm×5μm, 3μm×3μm, and 2μm×2μm capacitors using the CCM method. (p. 60)

Fig. 5-5 Equivalent circuit associated with the CCM technique, including the parasitic capacitance (C_{para}) of the probe station. (p. 61)

Fig. 5-6 Voltage buildup vs parasitic charge $Q_{\text{para}}(t) = I_0 \times t$, for various charging currents. (p. 62)

Fig. 5-7 Parasitic capacitance determined from the voltage buildup using $V(t) = (I_0 \times t)/C_{\text{para}}$, for various charging currents. (p. 62)

Fig. 5-8 Hysteresis plots of 100 μm×100 μm, 50 μm×50 μm, 20 μm×20 μm, 10 μm×10 μm, 5 μm×5 μm, 3 μm×3 μm, and 2 μm×2 μm capacitors obtained using the CCM technique with parasitic correction. (p. 63)

Fig. 5-9 Linear dielectric constant vs the size of the capacitor. Solid and open circles represent the dielectric constants obtained from the high-field slope of the hysteresis loops with and without parasitic correction, respectively. Full and

open squares represent the results measured using an LCR meter at 1 kHz and 10 kHz, respectively. (p. 63)

Fig. 5-10 Parasitic effect ($P_{BG} / P_{MAX,\mathrm{C}}$) on small-sized capacitors, where P_{BG} is the parasitic charge of the probing setup, and $P_{MAX,\mathrm{C}}$ is the maximum polarization charge with parasitic correction. The unbroken line is the expected result. The open circles and full squares represent the empirical results and the results obtained from ref. 6, respectively. (p. 64)

Chapter 6

Fig. 6-1 (a) Constant charging current (solid triangles) and triangular charging current (open circles) versus time. (b) Measured voltage profiles obtained using the CC (solid triangles) and TC (open circles) methods, for 250-nm-thick PZT(30/70) film. (p. 67)

Fig. 6-2 (a) Charging current-measured voltage characteristics obtained using CC (solid triangles) and TC (open circles) methods. (b) Polarization-voltage (P-V) plots obtained using CC (full line) and TC (open circles) methods. Area of sample was 10^{-4} cm^2. (p. 68)

Fig. 6-3 Polarization-voltage (P-V) plots obtained using TC method, for various step charging currents. (p. 69)

Fig. 6-4 Relation $t_\mathrm{S} = a / I_\mathrm{S}$ between the step charging time and the step charging current, where $a = 4.22 \times 10^{-12}$ is constant. (p. 70)

Fig. 6-5 (a) Measured voltage profiles and (b) polarization-voltage (P-V) plots obtained using TC method, for various numbers of charging steps. The maximum testing current and cycle duration were fixed at 40 nA and 0.69 s, respectively. (p. 70)

Fig. 6-6 Parasitic effect of probe setup: charging current versus measured voltage (open circles), and parasitic charge Q_{para} versus voltage (solid squares) obtained using TC method. (p. 71)

Fig. 6-7 Hysteresis plot of $3\mu m \times 3\mu m$ capacitor obtained using TC method with (solid line) and without (open circles) parasitic correction. (p. 72)

Fig. 6-8 (a) Capacitance-voltage characteristics of MIS capacitor. Open circles represent the measured result at 100 kHz. Red and Blue lines represent ideal C-V curves of high frequency and low frequency, respectively. (b) The leakage current-voltage characteristic of this capacitor with 5.0 nm-thick SiO_2. (p. 73)

Fig. 6-9 (a) Charging current versus measured voltage (open circles). (b) Polarization-voltage curve of MIS capacitor with 5 nm-thick SiO_2. Open squares represent the experimental P-V curve. Pink line represents result of ideal one. Blue dash lines represent the auxiliary line of the result with C_{Acc} = 60.1 pF. (p. 74)

Fig. 6-10 Capacitance-voltage characteristics of MFIS capacitor for various sweeping biases. (p. 75)

Fig. 6-11 Polarization charge of MFIS capacitor obtained using TC method for various biases. Purple lines represent the auxiliary line of the result with C_{Acc} = 93.3 pF. (p. 76)

Fig. 6-12 Memory window of MFIS stack obtained from P-V (full squares) and C-V (open squares) curves for various biases. (p. 77)

Fig. 6-13 Polarization-voltage (P-V) plots obtained using TC method, for various numbers of charging steps. The step charging time was around 4.3 ms. The number of charging step was changed from 100 to 400. The maximum testing current and the frequency of single cycle were changed from 4.8×10^{-8} A to 1.2

$\times 10^{-8}$ A and from 2.34 Hz to 0.58 Hz, respectively. (p. 78)

Fig. 6-14 Leakage current of PZT capacitors measured at various temperatures. The delay was around 1 s. (p. 78)

Fig. 6-15 Polarization-voltage loops of PZT capacitors measured at high temperature of 125 ^{o}C, for the various number of charging step. (p. 79)

Fig. 6-16 Polarization-voltage loops of PZT capacitors measured at different temperature, for the number of charging step of 100. (p. 80)

Chapter 7

Fig. 7-1 Full-switching current characteristics of ferroelectric films for various sweeping delay time. (p. 82)

Fig. 7-2 Triangular applied voltage (open circles) and hysteresis switching current (unbroken line) versus time, for 250-nm-thick PZT(30/70) film. (p. 84)

Fig. 7-3 Discharging current (I-t) characteristics for various holding voltage. The insert represents the leakage current-voltage plot obtained from I-t plots at the discharging time of 100 s. (p. 85)

Fig. 7-4 Polarization-voltage (P-V) plots obtained using virtual ground method (open circles) and I-V measurement method (unbroken line). Area of sample was 10^{-4} cm^2. The frequency of VG method and I-V measurement method are around 5.6 Hz and 0.1 Hz, respectively. (p. 86)

Fig. 7-5 Hysteresis loops of ferroelectric capacitor measured by RT66A. Black line represents the P-V curve measured at slow mode (~ 5.6 Hz). Blue line represents the result measured at fast mode (~ 56 Hz). (p. 86)

Fig. 7-6 Frequency-dependent coercive voltage plot of ferroelectric capacitor obtained from our previous results using the TC method. (p. 87)

Fig. 7-7 Voltage wave forms for full-switching and non-switching current

measurements. The poling time and remained time were about 5 ms and 10 s respectively. (p. 87)

Fig. 7-8 Switching current characteristics of ferroelectric capacitor for various poling voltage. (p. 88)

Fig. 7-9 Polarization charge density of ferroelectric capacitor for various poling voltage. The full-switching density and non-switching charge density are about 44.185 and 14.01 μC/cm^2, respectively. (p. 89)

Fig. 7-10 Voltage wave forms for retention polarization measurements. The poling time was about 5 ms and the remained time was changed from 1 s to 3000 s. (p. 90)

Fig. 7-11 (a) Positive half-hysteresis switching current characteristics and (b) its polarization-voltage (P-V) plots, for various remained time. (p. 91)

Fig. 7-12 (a) Negative half-hysteresis switching current characteristics and (b) its polarization-voltage (P-V) plots, for various remained time. (p. 92)

Fig. 7-13 Non-volatile polarization (ΔP^+ and ΔP^-) versus remained time plot (retention property) obtained using I-V measurement method and pulse polarization method, for 250-nm-thick PZT(30/70) film. (p. 92)

Fig. 7-14 Voltage wave form of de-polarization measurement. The poling time and remained time were about 5 ms and 10 s respectively. (p. 93)

Fig. 7-15 Switching current characteristics for various de-poling voltage, for 250-nm-thick PZT(30/70) film. The insert represents non-volatile polarization (ΔP) versus de-poling voltage plot. (p. 94)

Fig. 7-16 Leakage current characteristics measured at various temperatures, for 250-nm-thick PZT(30/70) film. The delay time of this measurement was about 1 s. (p. 95)

Fig. 7-17 Switching current characteristics measured at various temperatures, for 250-nm-thick PZT(30/70) film. (p. 95)

Fig. 7-18 Polarization-Voltage loops obtained at various measurement temperatures, for 250-nm-thick PZT(30/70) film. (p. 96)

Fig. 7-19 Testing profiles for (a) non-switching hysteresis current characteristic and (b) full-switching hysteresis current characteristic. (p. 97)

Fig. 7-20 (a) Full-switching hysteresis current characteristics and (b) non-switching hysteresis current characteristics measured at the temperature of 125 ^{o}C, for 250-nm-thick PZT(30/70) film. (p. 97)

Fig. 7-21 $q^{i}(t,V)$ - voltage plot of ferroelectric capacitor obtained at the measurement temperature of 125 ^{o}C, for 250-nm-thick PZT(30/70) film. (p. 98)

Fig. 7-22 Corrected ferroelectric hysteresis loops measured at various temperatures, for 250-nm-thick PZT(30/70) film. (p. 98)